ISIJ International, Vol. 62 (2022), No. 9, pp. 1896–1907
https://doi.org/10.2355/isijinternational.ISIJINT-2022-100

Analysis of Process Signals of Resistance Spot Welding for DP590 Steel Using Numerical Calculation

Kang ZHOU,[1)]* Gang WANG,[1)] Wenxiao YU,[1)] Huan LI[2)] and Mikhail IVANOV[3)]

1) School of Mechatronical Engineering, Beijing Institute of Technology, Beijing, China.
2) School of Mechanical Engineering, Yangtze University, Jingzhou, China.
3) Department of Welding Engineering, Institution of Engineering and Technology, South Ural State University, Chelyabinsk, Russia.

(*Received on March 14, 2022; accepted on May 29, 2022; J-STAGE Advance published date: June 30, 2022*)

Although the finite element (FE) numerical calculation model has been extensively employed in analyzing metal characteristics, very few works use it to analyze features of the main process signals during the resistance spot welding (RSW) process. Hence, its generality was seriously restricted. In this work, a 2D FE model, which coupled thermal, electrical and mechanical fields, was established with reasonable meshing and parameters and boundary conditions. The parent metal used dual phase (DP) 590 steel, which is commonly employed in automobile lightweight manufacturing process. An actual experiment with the same conditions as the numerical calculation was conducted. The dynamic resistance and electrode displacement obtained from numerical calculation and actual experiment were seriously compared and analyzed. Many important characteristics of process signals have been reasonably explained by combining the results obtained from numerical calculation and experiments. The reasonability and accuracy of the FE numerical calculation were not only verified after the welding process but also examined in depth during the intermediate welding process. Hence, the work can effectively enlarge the applications of the FE model and strengthen the correlation between control strategy design, online quality estimation using main process signals and FE numerical calculation during the RSW process.

KEY WORDS: resistance spot welding; FE numerical calculation; dynamic resistance; electrode displacement; electrode indentation.

1. Introduction

Resistance spot welding (RSW) has been extensively employed on various industrial production occasions, especially in bodies and frames of automobiles.[1)] At present, over 90% of assembly work for a car body is completed by RSW,[2,3)] and typically, a modern car body includes approximately 5 000 spot welds.[4)] Recently, dual-phase (DP) steel has been a type of newly developed sheet material to adapt to the lightweight and safety requirements of vehicles, due to it possesses many advantages of high strength, good corrosion resistance and punching characteristics, and has been gradually applied to modern car body manufacturing.[5)] Hence, exploring the weldability of DP steel and analyzing the characteristic variations during the RSW process have increasingly become one of current research hotspots in this area, not only for academic research on RSW process improvements, but also for actual industrial applications and promotions of automobile lightweight manufacturing process.

In recent years, many scholars have conducted various experiments to explore the features of DP steels during the RSW process.[6)] However, although many valuable conclusions have been drawn through various process parameter combinations, the conclusions may lack enough generality. To save experimental costs and obtain more general conclusions, one commonly-employed numerical calculation tool, which is the finite element (FE) method, has been increasingly used in analyzing the RSW process characteristics or improving the welding schedule.[7–9)] Using the FE numerical calculation tool, many transient characteristics, such as temperature and stress variation, which cannot be accurately collected by corresponding sensors, can be employed to deeply explore physical or other aspects' information during the welding process. However, the majority of related works have focused on metal characteristic variations under the effects of various coupled physical fields, and very few works have concerned the characteristics of process signals.

* Corresponding author: E-mail: zhoukang326@126.com

Under these circumstances, the comparison between numerical calculation and actual experimental examination results can only be conducted during the post-processing stage, which significantly deteriorates reference and instruction roles of numerical calculation for the actual experimental or production process. Additionally, because a comparison during the intermediate process was lacking, the results obtained from the FE method could not be accepted during many actual application occasions.

The goal of RSW operation is to obtain welds with satisfactory quality. To achieve this goal, a proper control strategy should be employed.[10] Although there were only three main controllable parameters, electrode force, welding current and welding time, which existed during the process, a proper welding schedule should be seriously considered by examining and analyzing so many process information. In general, some important process signals, such as dynamic resistance and electrode displacement, are commonly employed on many occasions because they can indirectly reflect the physical characteristics of the parent metal sheets.[11,12] For decades, these two signals were always medium process variables to accomplish the nondestructive test (NDT) task[13,14] or design a tracking control strategy.[15] However, there were few works concerning obtaining these two signals by means of numerical calculation, so the works cannot be closely related to the actual engineering requirements.

In this work, numerical calculation using the FE method was conducted for a medium frequency DC RSW process, and the parent metal sheet used DP590 steel sheets, which is commonly employed in modern lightweight car design and manufacturing.[15] Unlike exploring the material characteristics only through the comparisons of the post-processing results, the characteristics of intermediate process variables, such as dynamic resistance and electrode displacement, were explored in depth, which can seriously study the characteristic variation in real time during different stages of the welding process. Additionally, the final nugget pattern and other features were considered. It can largely expand the examination or comparison range. The work focused on how to make accurate correspondence between numerical calculation results and actual experimentally collected results. The RSW experimental operational process included so many uncertainties,[16] while the numerical calculation might have difficulty in accurately setting the parameters for this multi-field coupling process. Therefore, an important conduction in this work was to improve or optimize both experimental and numerical calculation processes. It is anticipated that the work can strengthen the relation between numerical calculation and actual experimental operation, so make the numerical calculation well serve and instruct actual experimental or engineering application.

2. FE Model Establishment of a RSW Process

To achieve the goal of analyzing the intermediate process variables during different stages of the welding process, a more sophisticated and accurate FE model should be used in this work. Unlike the commonly used model which can only be used to analyze the material characteristics during the post-processing stages, the model in this work should take some special measures. For example, a much denser mesh should be employed, and the contact areas and contact resistances between parent metal sheets and electrodes should be seriously considered in the model establishing and analysis process.

During the RSW process, two separated parent metal sheets were pressed between upper and lower electrodes by preliminarily setting the electrode force, so there were a total of three contact surfaces. In addition, welding currents went through the electrodes and parent metal sheets, and then heat was generated from the interface between parent metals and spread to nearby zones. To protect the electrodes, cooling water was added by delivering cooling water to the electrode cavity so that the heat generated from the interface between the electrodes and parent metal sheets could be quickly removed. Because the welding process was very short, radiant heat transfer might not be considered. However, to guarantee the consistency between model establishment and actual experiment, the heat convection between surfaces of parent metal sheets and electrodes, and surrounding air, as well as the heat convection of different sections of surfaces of pipe with cooling water, was seriously considered in this work. Moreover, the electrodes and parent metal sheets were assumed to be isotropic and homogeneous materials, and followed the von-Mises yield criterion and bilinear isotropic (BISO) hardening criterion. The magnetic effects generated from the electrical current, as well as the flow and convection of liquid metals were not considered in this work. **Figure 1** shows a physical illustration of the RSW process for DP590 steel sheets.

It can be clearly shown that the electrode force and welding current were externally imposed effects, and together with the corresponding welding time duration, an integrated welding schedule was constituted.

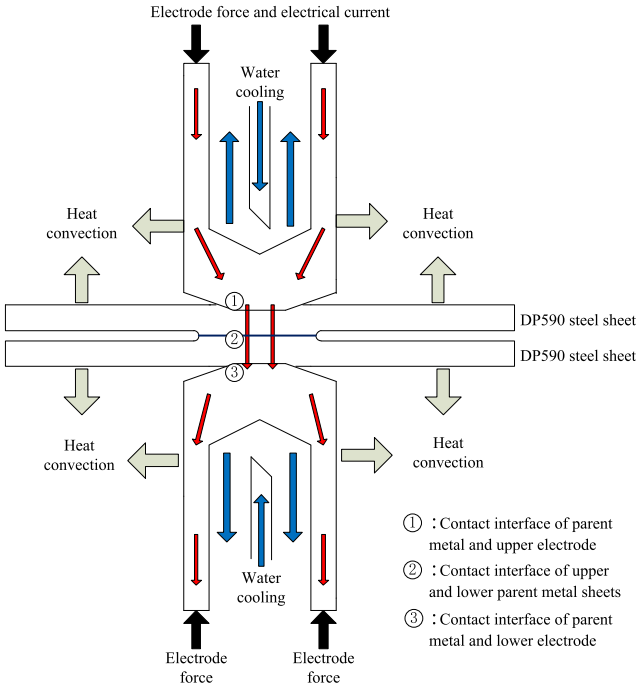

Fig. 1. A physical illustration of the RSW process for DP590 steel sheets. (Online version in color.)

2.1. FE Model and Boundary Conditions

RSW process is a multi-field coupled process. In this work, a numerical calculation model was established based on a thermo-electrical coupled field, and then superimposed on a mechanical field, which can sufficiently reflect the main process characteristic variation of an RSW operational process and avoid complex process analyses and coupled calculations. Although some other elements, such as electromagnetic stirring and fluid flow behaviors,[7,9] can also affect the phase transition and nugget formation, they had limited effects on the characteristic variations of process signals during this very short time and might not be considered in this work. Therefore, the FE model in this work only considered the thermal field, mechanical field, electrical field and their coupled effects during the RSW process.

Considering a common symmetrical characteristic of common RSW operation, a 1/2 axisymmetric two-dimensional (2D) FE model was established by a commercial software, ANSYS12.1. The model was a thermal-electric-mechanical coupled model. This FE model and corresponding meshing presentation are shown in **Fig. 2**.

The *x* axis in Fig. 2 denotes a horizontal direction, while the *y* axis denotes a vertical direction. The mesh densities in different parts of the model were remarkably different. To more clearly simulate the characteristic variation of parent metal sheets during the welding process, the zone of parent metal sheets had a much denser mesh. On the other hand, the zone far away from the parent metal sheets had a gradually sparse mesh, which can improve the efficiency of the numerical calculation. Because the electrodes had a pipe with cooling water, the effect of temperature variation on the electrodes was relatively small; hence, a very sparse mesh in this zone was sufficient. The model in Fig. 2 employed a 2D 8-node element (PLANE183) to conduct the mechanical field analysis, and employed another 2D 8-node element (PLANE223) to analyze the thermo-electrical coupled field.

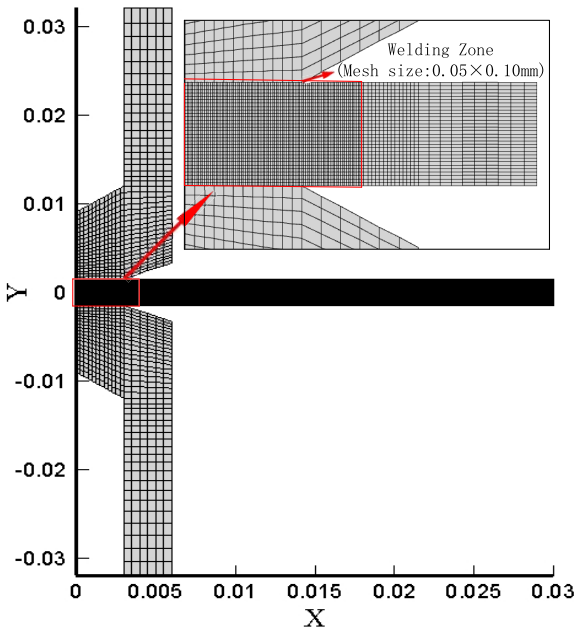

Fig. 2. 1/2 axisymmetric thermal-electric-mechanical coupled FE model and corresponding meshing presentation. (Online version in color.)

Three contact surfaces included three contact pairs, and each pair can be represented by a 2D 8-node surface-to-surface contact element (CONTA172) together with a 2D target segment (TARGE169). These three contact surfaces were considered surface-to-surface contacts, and the coefficient of friction was set to be 0.05, which was set by means of several trials combining corresponding operational experiences. The corresponding contact algorithm employed the augmented Lagrange method because this method usually led to a better conditioning and was less sensitive to the magnitude of the contact stiffness.[17] In addition, the model included a total of 5 976 elements, and the mesh size in the welding zone was 0.05 mm×0.10 mm, which was enough to achieve high computational accuracy with a high reliability. Moreover, the maximum aspect ratio for this model was 8.3, which appeared on the top of the two electrodes, because this area was far away from the welding zone and its effect on the numerical calculation could be ignored. In the welding zone, the maximum aspect ratio was 2.0, which was enough to meet the requirements of a high calculation accuracy and reliability. Furthermore, the quality of the mesh in this model was checked using the mesh check function inside the software, and no error element or warning was found, which can ensure the accuracy and reliability of the following numerical calculations. The Jacobian ratios of all the elements in this model were below 1.1, and all the distortion values were within a reasonable range.

This FE model included two electrodes and two parent metal sheets. The width of the parent metal sheets was 1.5 mm, the length was 30.0 mm, and the material characteristics used the parameters of DP590 steel. The material of the upper and lower electrodes used Cu–Cr–Zr alloy, and a particular electrode geometry used in this work was a truncated cone with a 120° angle and a 6.0 mm face diameter. The diameter of the electrode was 13.0 mm, the overall height was 32.0 mm, and the diameter of pipe with cooling water was 6.0 mm. Corresponding material characteristics were employed to conduct the model calculation, which included mechanical characteristics such as Young's modulus and yield stress, physical characteristics such as density, thermal conductivity, thermal expansion coefficient and specific heat capacity, as well as the electrical characteristics such as electrical conductivity.[18,19] In addition, considering the relation between the latent heat and enthalpy of the parent metal sheets, the latent heat value, which was 2.72×10^{-5} J/Kg,[20] was combined into the enthalpy setting. Moreover, the tangent modulus of the electrode was respectively 1 800 MPa.[17] Furthermore, because the temperature of the electrodes had no significant variation due to the effect of cooling water, Poisson's ratio was set to a constant, which was 0.32.[21] On the other hand, the temperature of the parent metal sheet may have a significant variation, corresponding tangent modulus of the parent metal sheet should be 20 MPa-2 100 MPa with different temperatures,[19] and the Poisson's ratio should also be a varying data with different temperature, which was 0.29–0.33.[22] Because the majority of material characteristics vary with temperatures, to obtain sufficient and reliable characteristic data, parts of the data used adjustment and linear interpolation.

In addition, some important boundary conditions were required to be seriously set. An external electrode force

was applied on the top of the upper electrode, while the displacement along the y direction of all the nodes of the lower upper electrode was constrained. Additionally, considering the axisymmetric characteristics of the metal deformation during the welding process, for nodes along the y axis, their displacements along the x direction were also constrained. For other boundaries, no stress constraint was applied. In addition, heat convection coefficients should also be set. For the heat convection of different sections of surfaces of pipe with cooling water, the coefficient was set to be 3 800 W/(m^2•°C) when the temperature of cavity of electrode was below 100°C, when the temperature was above 100°C, corresponding coefficient was set to be 20 000 W/(m^2•°C).[23] For the heat convection between air and surfaces of parent metal sheets and electrodes, corresponding coefficients varied with the temperature. The environmental temperature was 25°C, and all the boundaries were set to be adiabatic. Moreover, the degree of freedom of voltage of all the nodes in the top surface of the upper electrode was coupled to the applied external welding current. On the other hand, the voltage of all the nodes in the bottom surface of the lower electrode was constrained to 0 V. **Figure 3** shows corresponding boundary conditions of the model used in this work.

2.2. Physical Fields Used in the Model

This model involved a thermo-electrical coupled field and a mechanical field. These two parts was coupled each other in this work. The function of the mechanical field was that under the effect of electrode force on the parent metal sheets, the stress and strain of each node could be calculated, and then the displacement increment of the nodes, stress increment resulting from the external load, contact statuses of the nodes, and other relative information could also be obtained. Then the thermo-electrical coupled model could utilize this information to calculate the electrical resistance along the welding current direction, so the corresponding current density could be updated, and then the parameter information of the electrical and temperature fields were also updated.

The FE calculation of the mechanical field should follow two equations:

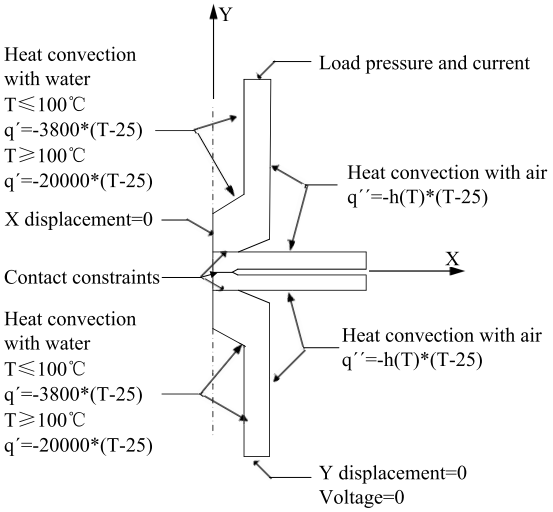

Fig. 3. Boundary conditions of the model.

$$d\sigma = D_{ep}d\varepsilon - C_{ep}dT. \quad \text{..... (1)}$$

where $d\sigma$ and $d\varepsilon$ are the stress increment and strain increment, respectively, D_{ep} is the elastic matrix, C_{ep} is the elastic temperature vector, and T is the temperature. Equation (1) was a constitutive equation; apart from this equation, there was another stiffness equation:

$$K^e da^e = dp^e + dp_T{}^e. \quad \text{..... (2)}$$

where K^e is a unit stiffness matrix, da^e is the node displacement increment, and dp^e and $dp_T{}^e$ are respectively equivalent node stress increments resulting from variations in load and temperature.

The analysis of thermo-electrical coupled model during the RSW process was a typical issue of transient heat transfer from the internal heat source. Through corresponding numerical calculations, the variations in material characteristics and microstructures, heat generation, distributions of temperature and electrical parameters, and other relative information can be obtained. The transient heat transfer control equation in the 2D environment was as follows:

$$\rho c\frac{\partial T}{\partial \tau} = \frac{\partial}{\partial x}\left(k\frac{\partial T}{\partial x}\right) + \frac{\partial}{\partial y}\left(k\frac{\partial T}{\partial y}\right) + Q. \quad \text{..... (3)}$$

where ρ is the density of the material, c is the specific heat capacity, τ was the time, k is the thermal conductivity and Q denotes the latent heat.

2.3. Heat and Electrical Contact

During the numerical calculation for the RSW process, calculations of electrical contact conductance (ECC), thermal contact conductance (TCC), and contact resistance, significantly affected the temperature distribution in the weld zone, and further remarkably affected other relative numerical calculation results. This was because the ECC and TCC may affect the temperature distribution, which can further affect the nugget size, resistivity, yield stress and other relative material characteristics, so the variations of dynamic resistance and electrode displacement can also be seriously affected. In addition, under the effect of electrode force, the contact areas of the three contact surfaces were affected by the temperature distribution, so the corresponding contact resistances and the amounts of heat between the interfaces of the parent metal sheets were also affected. This heat can in turn affect the temperature distribution in this zone, as well as the calculation values of dynamic resistance and other relative items. Moreover, the heat generated in the welding zone can make the parent metal sheets move because of linear thermal expansion, so the calculations of electrode displacement and electrode indentation were affected. Hence, it can be inferred that the accuracy of the ECC and TCC may affect the reliability of the calculation results of nugget size, dynamic resistance, electrode displacement, contact area, and electrode indentation.

Contact resistance can significantly influence many aspects of the RSW process, such as nugget formation and growth processes, temperature distribution.[24] The bulk resistance increased as the temperature increasing and was almost irrelevant to the electrode force. However, the contact resistance was sensitive to the temperature, electrode force and surface condition of the contact surfaces. The

calculation of the contact resistance in environmental temperature can follow Eq. (4):

$$R_c = r_c F^m. \quad \text{..... (4)}$$

where R_c is the contact resistance, r_c is the contact resistance when the electrode force is 1 N, F is the contact force, which varies during the welding process, so its value should be obtained according to online corresponding calculation, and m is the thin film factor, which is relative to the material property and surface condition. In this work, the r_c between parent metal sheets was set to be 2.75×10^{-2} Ohm, and this value between parent metals sheet and electrodes was set to be 1.375×10^{-2} Ohm, and the m was set to be -0.7, according to a previous contribution.[25)]

During the RSW process, the contact resistance between parent metal sheets and electrodes can make the temperature at their interfaces increase, so Eq. (4) cannot be applied at a high temperature. A corresponding a modifying equation which considers the condition of high temperature was applied as follows:

$$R_c = \frac{r_c \rho_T}{\rho_{25}} X(T) F^m. \quad \text{..... (5)}$$

where ρ_{25} and ρ_T are the average resistivity of the two contact materials under environmental conditions and current temperature T, respectively, and $X(T)$ is a modifying coefficient, which is relative to the yield stress of the two contact materials, in this work.

The contact area was calculated before calculating the contact force. During the process of calculating the contact area, the element deactivation/reactivation procedure in the mechanical field model should be used to calculate the number of contact elements between two parent metal sheets, and then a control area of each contact element should be obtained. In this 2D model, the area can be described using the length of the contact line between two contact elements. Because the number of contact elements varied and the current density at each contact element changed, the pressure at the element also varied. Therefore, when calculating the contact force within a contact surface, it was assumed that the contact surface between two parent metal sheets included n contact elements, and d_i, which was the length of the contact line of the ith contact element, was used to be the width of the corresponding ring which can be used to calculate its area S_{ci} and pressure P_i of this contact element.

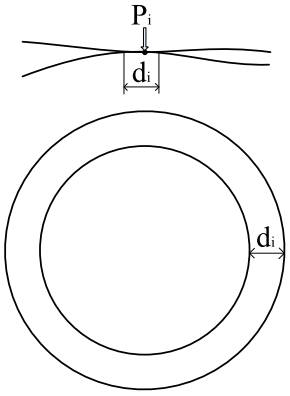

Fig. 4. Schematic of length of contact line and pressure. (Online version in color.)

Figure 4 shows the corresponding schematic of the length of the contact line and pressure.

Then, the contact force F can be calculated as follows:

$$F = \sum_{i=1}^{n} \left(P_i S_{ci} \right). \quad \text{..... (6)}$$

According to Eqs. (4)–(6), contact resistance under different temperatures can be obtained. In ANSYS software, ECC was employed to denote the electrical characteristics of the contact surface, and the relation between the ECC, contact resistance R_c and contact area S_c, can be described as follows:

$$ECC = \frac{1}{R_C S_C}. \quad \text{..... (7)}$$

At the initial stage of the welding process, the temperature difference between the parent metal sheets and electrodes was very small, so the effect of TCC on the welding process was so small. At the mid-late stage of the process, the temperature difference was increased; at the same time, the increased temperature of the parent metal sheets softened the surface of the parent metal sheets, so three contacts between the parent metals and electrodes were much closer under the effect of electrode force, which induced lower thermal contact resistance (TCR) and higher TCC. In general, this parameter setting had so few effects on the weld nugget formation, so in this work, after studying some previous works,[2,26)] this value was set as 1.0×10^7 W/(m^2•°C).

Hence, during the numerical calculation process, using above corresponding equations can calculate the ECC, and set a proper value of TCC; then, the voltage and temperature of the contact node can be obtained. However, according to review previously published contributions, there were some serious problems when using the corresponding FE model to simulate the process. Although the effects of temperature and electrode pressure on contact resistance were considered, Wan *et al.*[26)] used a fixed contact pressure when calculating the contact resistance. However, the contact area, number of contact nodes and current distribution of the current density varied, which induced the contact pressure to vary during an actual welding process. Zhao *et al.*[27)] and Zhang[28)] used an average pressure of the nodes to replace the contact pressures; however, this can induce more errors because the contact pressure of different nodes had more differences. In addition, in some previous works,[6,20,29)] the mesh was so sparse in some key zones, which made the calculation of contact area inaccurate and deteriorated the accuracy of the calculations. Because some contributions may not seriously consider all conditions setting during the calculation, as well as other simplicities, such as no considering the friction between different contact surfaces, setting the density of metal to be a constant without considering the temperature variation, the numerical calculation and simulation results of nugget size and other key process variables had more errors, which significantly limited the generality and consistency of the model calculation and simulation results.

2.4. Model Calculation

In the model used in this work, many cycles were included. Each cycle was composed of two steps. The first step was applying the load of electrode force in the

mechanical field model to calculate corresponding variable information of the nodes, such as displacement, contact area and contact force, and then transferred the results to the thermo-electrical coupled model. In the thermo-electrical coupled model, the ECC was calculated by means of the contact area and contact force calculated in the previous step, and then the temperature and voltage of the nodes were calculated. These two steps corresponded to their individual databases, which included their individual model information and calculation results, so the two steps constituted an initial couple of thermo-electrical-mechanical fields. Then, a cycle calculation was carried out. The mechanical field model was again calculated based on the initial coupled results, and then the thermo-electrical field model was calculated based on the preceding calculation results of the mechanical field model so that the ECC could be updated. Then, the mechanical field model can be again calculated based on the updated temperature information. So an integrated cycle calculation could be conducted. The number of cycles was determined by the total simulation time. In this work, one cycle corresponded to 0.002 s of welding time, and the total welding time lasted 0.30 s, so a total of 150 cycles were required. **Figure 5** shows the integrated multi-field coupled calculation process.

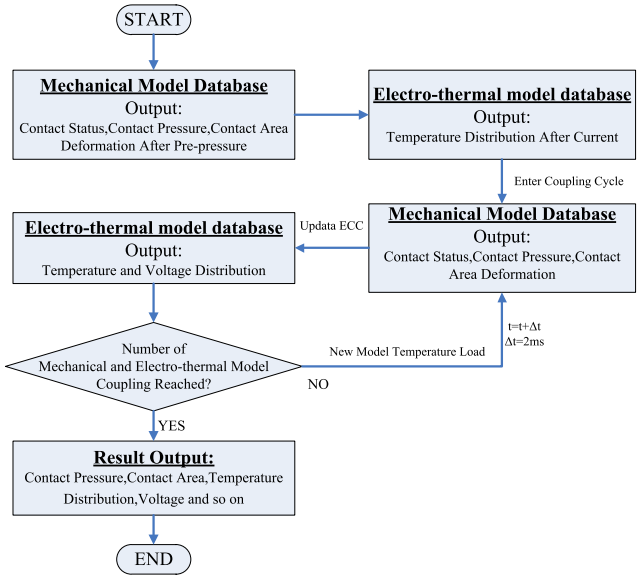

Fig. 5. Calculation procedure of the multi-field coupled FE model. (Online version in color.)

3. Experiment and Verification

3.1. Experimental Platform and Facility

To verify the effectiveness and accuracy of this multi-field coupled FE model, an actual experiment with the same conditions as those of the FE model was conducted. In the experiment, two DP590 steel sheets with 200.0×25.0×1.5 mm in size were employed as parent metal sheets. The distance between two adjacent welds was approximately 20.0–30.0 mm. **Table 1** shows the material characteristics of the parent metal sheets.

The electrode compositions and shape were the same as those used in the FE model. The corresponding process parameters are shown in **Table 2**.

The welding machine used an 80 kVA three-phase medium frequency DC RSW machine with a special controller MF-3000-02 with a human-computer interaction interface, and the control frequency was 1 000 Hz. Some special data collection facilities were used. A MEATROL Rogowski current transducer with 0.5% accuracy was employed to online measure the welding current, while a MILONT G25-5 LVDT sensor was used to detect the displacement of the upper electrode online, and its measurement range and resolution were 5.0 mm and 6.0 μm, respectively. Corresponding data acquisition card used a PCI-6251M series 16 digital collection integrated circuit board manufactured by NI Corporation, and the sampling frequency was 4 kHz. A personal computer was used to storage the data and process the voltage, current and electrode displacement signals by means of a data collection and processing program developed by LABVIEW 2018. The corresponding synchronous data collection and processing facility is shown in **Fig. 6**.

During each welding operation, to obtain effective signals with a high accuracy, before the formal welding experiment, several tests were conducted to obtain the mean values of electrode displacement vibrations, so that the actual collection values could be amended in formal experiments. Additionally, a special electromagnetic shielding was employed to assure the accuracy of the collection of electrode displacements using the LVDT sensor. In addition, the welding current was an input variable to the welding controller, and its setting should coincide with that in the numerical calculation. **Figure 7** shows the welding current profiles during the actual RSW experiment and numerical calculation processes.

Table 1. Material characteristics of the DP590 steel sheet used in this work.

Material	Chemical composition (mass%)					Mechanical property		
	C	Mn	Si	S	P	Yield Strength (MPa)	Tensile Strength (MPa)	Elongation (%)
DP590 steel	0.13	2.36	0.60	0.015	0.04	355	590	20

Table 2. Process parameter of the welding experiment.

Material	Surface state	Thickness (mm)	Welding Schedule		
			Current (kA)	Electrode force (N)	Welding time (s)
DP590 steel	Bare	1.50+1.50	8.50	4 500.00	0.30

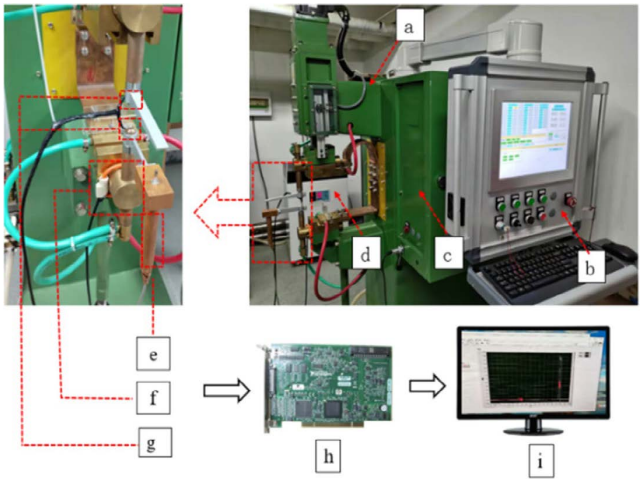

Fig. 6. Synchronous data collection and processing facility. , (a) welding machine, (b) human-computer interaction interface, (c) welding controller, (d) water cooler equipment, (e) LVDT sensor, (f) Rogowski current transducer, (g) wire for voltage measurement, (h) data acquisition card, (i) data collection and processing program (Online version in color.)

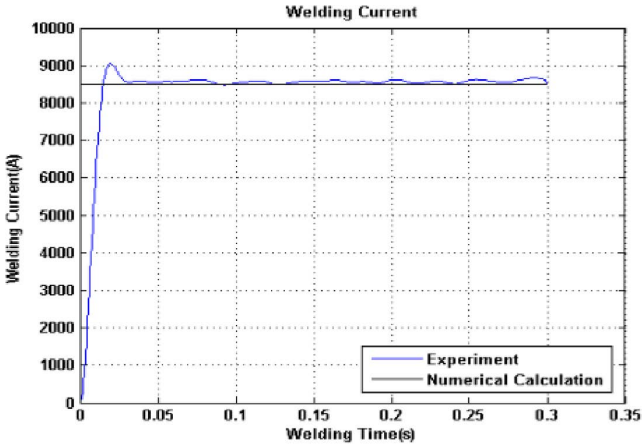

Fig. 7. Welding current profiles used in the experiment and numerical calculation. (Online version in color.)

In this part, actual process variables, such as dynamic resistance and electrode displacement, were compared between the numerical calculation and actual experimental data. Additionally, other important relative parameters, including electrode indentation and nugget profile, were used to verify the effectiveness and reliability of the FE model and experiment. By means of a series of comparisons and analyses, more key characteristics can be obtained, and further explorations and conclusions can be drawn.

3.2. Dynamic Resistance

The dynamic resistance was very important because it was directly related to the heat generation in the weld zone. During the RSW process, the heat generation followed the equation:

$$Q_H = I^2 Rt. \quad \text{..... (8)}$$

where Q_H is the heat generated during the process, I is the welding current, R is the resistance between the upper and lower electrodes, which is called the dynamic resistance because its value was varying during the process. According to Fig. 7, the welding current, which should be a DC welding current with an approximate constant value, had no remarkable change because a constant current control strategy, which is the most commonly-employed and effective control strategy, was employed,[30] and t is also a predestined value, so R can determine the amount of heat to melt the parent metal sheets. This parameter can be used not only to monitor the nugget formation and growth process but also to assist in designing or optimizing proper welding schedules.

To obtain accurate and reliable dynamic resistance during the experiment, all the parent metal sheets were processed using fine abrasive paper to remove the rust, oil stain and oxide layer, and then cleaned with 98% alcohol. During the numerical calculation process, in general, dynamic resistance can be described as follows:

$$R = R_b + R_c. \quad \text{..... (9)}$$

where R_b is the bulk resistance. In Section.2.3, Eq. (5) is used to calculate the contact resistance R_c. In that equation, $X(T)$ is the modify coefficient. In this work, following processing method is used.

$$X(T) = \frac{\sigma_T}{\sigma_{25}}. \quad \text{..... (10)}$$

where σ_T is a minimum value of the yield stresses of the two contact materials when the temperature was T, while σ_{25} is the corresponding value when the temperature is 25°C.

According to deductions using the above equations, corresponding numerical calculations can be conducted to obtain the dynamic resistance during the welding process. Then, the results can be compared with the actual dynamic resistance collected and calculated by the actual experiments. **Figure 8** shows the two dynamic resistance curves obtained from the numerical calculation and actual experimental data collection and calculation.

According to Fig. 8, there were three main different stages in the curves, which followed the common senses of the characteristics of dynamic resistance.[31] In the first stage, the dynamic resistance sharply decreased. This was because under the effect of electrode force, the parent metal sheets were softened; hence, according to the calculation equation of contact resistance combining the setting parameter values, the contact resistance calculated by numerical calculation decreased. On the other hand, the surface of the parent metal sheets had various films, oxides, or various contaminants, and the electrode force could cause these contaminants to break up, which also induced the dynamic resistance to suddenly decline. Although other elements may make the bulk resistance increase, such as increasing temperature can make the resistivity of the parent metal sheets increase, at this moment, the contact resistance dominated the whole dynamic resistance, and the temperature only had a small increase. Therefore, both the dynamic resistance curves obtained from the experimental measurements and numerical calculations significantly decreased in this stage. Then, in the second stage, the dynamic resistance increased, which was mainly because the resistivity of the bulk resistance increased with increasing temperature. In the last stage, the dynamic resistance decreased. Because the nugget size continuously increased, the contact areas of the three contact surfaces also increased, and each sur-

face of the parent metal sheets remained squeezed so that mechanical crushing occurred, hence, electrode indentations on the surfaces of the parent metal sheets were increasingly obvious in this stage. **Figure 9** shows the diameter of the contact area between the electrodes and parent metal sheets obtained from the numerical calculation.

It can be observed from Fig. 9 that from 0.15 s of welding time, mechanical crushing began occurring at the contact surfaces between the electrodes and parent metal sheets, so the diameter of the contact area began increasing, in other words, the cross-sectional area between the electrodes and parent metal sheets continuously increased from this time. It can be found from both numerical calculation and experimental examination, the cone side on the tip of the electrodes contacted the parent metal sheets, where electrode indentation can be detected. The appearance of electrode indentation induced an increase in the contact area of the contact surfaces. The corresponding diameter of the contact area between the electrodes and parent metal sheets obtained from the actual experiment was 6.51 mm measured after the welding process, which corresponded to 0.30 s of welding time, while the corresponding value in the numerical calculation shown in Fig. 8 was 6.43 mm, and the error in percent form was within 1.23%. This meant that the numerical calculation approached the actual experimental measurement very much. On the other hand, from the time of 0.15 s to 0.30 s, the contact area increased 17.87%, which was also one of the main reasons for the dynamic resistance decreasing in this stage.

On the other hand, the contact between two parent metal sheets also should be seriously considered. When the welding process began and the electrode force was imposed and the temperature sharply increased, the stress generated from the parent metal sheets was so large that the terminals of the two contacted parent metal sheets were out of contact. **Figure 10** shows the displacement of the parent metal sheets along y direction at this stage when the welding time was 0.016 s.

As the welding time increased, the diameter of the contact area increased as the temperature increasing and nugget formation and growth occurred. **Figure 11** shows the diameter of the contact area from the numerical calculation during the process.

According to Fig. 8, the time when the dynamic resistance curves decreased to a minimum value at the beginning of the welding process was so approached the time when the diameter of the contact area between the two parent metal sheets reached its minimum value.

In addition, in the first stage, the dynamic resistance obtained from the experimental measurement was slightly lower than that from the numerical calculation. This may be because the numerical calculation cannot consider the

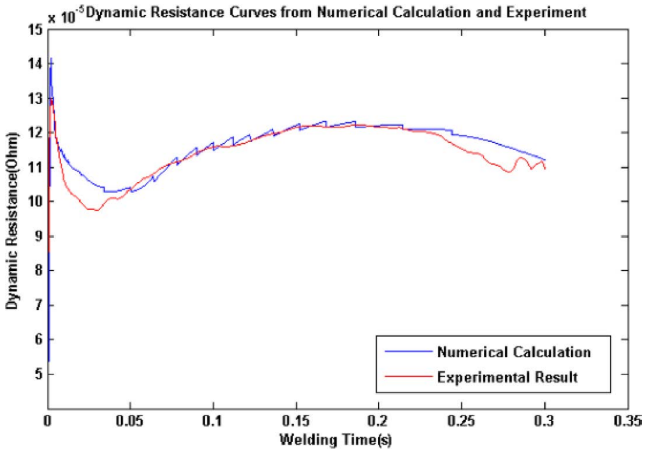

Fig. 8. Dynamic resistance curves from numerical calculation and experiment. (Online version in color.)

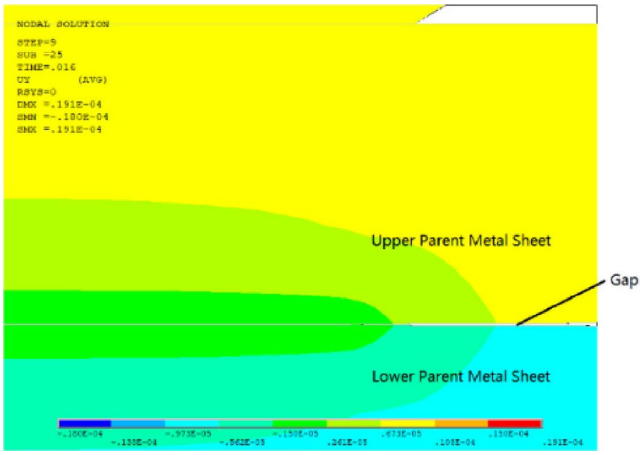

Fig. 10. Displacement of two parent metal sheets in y direction. (Online version in color.)

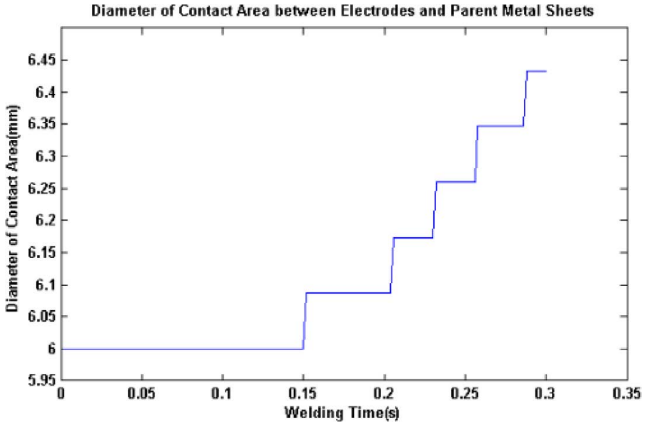

Fig. 9. Diameter of contact area between electrodes and parent metal sheets. (Online version in color.)

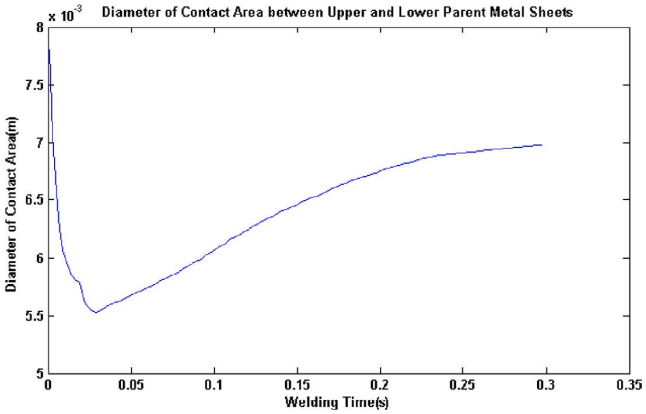

Fig. 11. Diameter of contact area between the upper and lower parent metal sheets. (Online version in color.)

surface uncertainties and contaminants of the parent metal sheets, which were the main elements inducing the contact dynamic resistances in reality. Additionally, at the beginning of the welding process using a medium frequency DC RSW machine, the welding current should achieve the predetermined value after a short time; moreover, a strong magnetic field during the process can interfere with the measurement of voltage, which was used to calculate the dynamic resistance. Furthermore, during the numerical calculation process, the parameter values might not be accurate at every temperature, which can also induce errors in the dynamic resistances obtained between the experimental measurement and numerical calculation.

3.3. Electrode Displacement

During the welding process, the electrode displacement changed for various reasons. The first was that the heat was generated in the welding zone, so increasing temperature could cause the parent metal sheets to generate linear thermal expansion, which followed Eq. (11):

$$\Delta L = \alpha L \Delta T. \quad \text{..... (11)}$$

where ΔL is the thickness increment of metal linear thermal expansion, α is the linear thermal expansion coefficient, L is the thickness of parent metal sheets, and ΔT is the temperature variation during the process. As the temperature increased, metal linear thermal expansion enlarged the volume of the parent metal sheets, and this expansion was a main reason for the upper electrode moving up. During the process, the linear thermal expansion coefficient of the parent metal sheets may increase with the increasing temperature; hence, different values of α were used in the numerical calculation so as to improve the accuracy of the calculation.

During the numerical calculation, the displacement of the bottom of the lower electrode was constrained. The displacement of the upper electrode should be considered by combining metal linear thermal expansion and electrode indentation. The corresponding mathematical description can be as follows:

$$S = 2\sum \alpha_{1i}\Delta L_{1i}\Delta T_{1i} + 2\sum \alpha_{2j}\Delta L_{2j}\Delta T_{2j} - 2S_{EF}. \quad \text{... (12)}$$

where S is the total electrode displacement, α_{1i} is the linear expansion coefficient of the parent metal sheet at different temperatures, ΔL_{1i} is the thickness of the parent metal sheet at different temperatures, ΔT_{1i} is the temperature gradient of the parent metal sheet during the welding process. On the other hand, α_{2i}, ΔL_{2i} and ΔT_{2i} were the corresponding parameters for the electrodes. In addition, S_{EF} was the electrode indention. During the numerical calculation, it was assumed that the upper and lower electrodes, as well as two contact parent metal sheets, had the same properties, so the corresponding expansion and movement were the same and symmetrical. Additionally, it can be found from Eq. (12) that the displacement can increase because of the metal linear thermal expansion, but can decline because of the electrode indention. **Figure 12** shows a comparison of the electrode displacements obtained from numerical calculation and experiments.

The two displacement curves approached each other. The maximum error of the two displacement curves is 4.15×10^{-5} m at 0.24 s, while the error is only 7.00% at the end

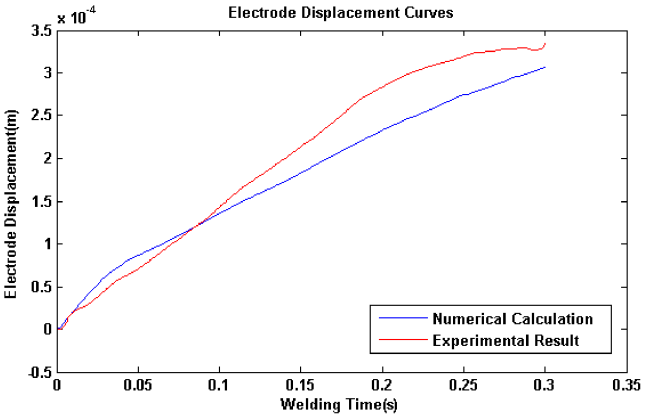

Fig. 12. Comparison of the electrode displacements. (Online version in color.)

of welding process. Because at the initial stage, the linear thermal expansion coefficients used in numerical calculation was so accurate, and as the temperature increasing, corresponding coefficients cannot set accurate values, the errors between numerical calculation and experimental results were comparatively large. In addition, at the end of the process, phase transition occurred and liquid nugget appeared, which might induce the coefficient decrease, so the error correspondingly was a bit smaller than before. To quantitatively estimate the similarity of two curves, a correlation coefficient was employed to reflect the level, and the corresponding calculation followed Eq. (13).

$$r(X,Y) = \frac{Cov(X,Y)}{\sqrt{Var[X]Var[Y]}}. \quad \text{..... (13)}$$

where $r(X,Y)$ is the correlation coefficient between X and Y, $Cov(X,Y)$ refers to the covariance of X and Y, and $Var[X]$ and $Var[Y]$ denote the variance of X and Y, respectively. In this work, X and Y are two curves shown in Fig. 12. The result of the correlation was 0.9976, which denoted that the similarity level of the two curves was very high, so the reliabilities of numerical calculation and experiment can be sufficiently verified. In addition, with the different amount of heat energy delivered into the welding system, the electrode displacement variation had three different situations. The first was electrode displacement kept rising, and the second was that the displacement rose a while and then remained steady with only a small variation, while the last was that after rose a short while, and then the curve slowly declined. For the first situation, it meant that the metal linear thermal expansion dominated the whole process and was above the electrode indentation, and the nugget size was continuously increasing, so kept delivery more external energy can obtain better and better welding quality. When the curve remained steady or declined, the electrode indentation may be equal to or above the metal linear thermal expansion. Under these two circumstances, keeping delivering more external energy may not be able to increase the nugget size, or expulsion may occur induced by a large electrode indention.[31)]

Expulsion is a universal problem and has potential damage to welding products and surrounding facilities.[32)] In general, various process signals can be used to detect whether and when it occurs online. In this work, dynamic resistance and electrode displacement were used to detect

expulsion, and their resolution was compared. To easily obtain expulsion during the process, the welding schedule was adjusted. Under the conditions of 4 000 N of electrode force and 0.40 s of welding time, expulsion occurred, and corresponding data were collected. **Figure 13** respectively shows the dynamic resistance and electrode displacement curves when expulsion occurred.

Figure 13 shows that the electrode displacement was more sensitive for detecting the expulsion than dynamic resistance, because at 0.26 s of welding time, when expulsion occurred, the decline in electrode displacement was more obvious than that of electrode displacement. However, a single signal might not be enough to detect the expulsion, to increase the accuracy of detecting the expulsion; it was suggested that the various process signals were synchronously employed.

During the welding process, there were various elements affecting the electrode displacement, such as the energy delivery vibration, and electrode worn. Under the condition of an equal amount of energy delivered into the welding system, energy delivery using DC format can obtain much steadier electrode displacement than that using the AC format.[17] In addition, the worn electrode can increase the contact resistance between the electrode and parent metal sheet, so the heat in the welding zone can also increase, which can increase the temperature of the surface of the parent metal sheets and can decrease the yield stress of the materials, so that a much deeper electrode indentation can be obtained. At the same time, it can also further damage the electrodes. Hence, for the electrode displacement, the peak value should be much lower than that using the normal electrode and the curve can quickly enter the decline stage. **Figure 14** shows the electrode displacement when the electrode was worn. To make the characteristics more obvious, the welding time was 0.40 s.

The peak value of the curve in Fig. 14 was 1.67×10^{-4} m, which was obviously smaller than that in Figs. 12 and 13(b). Deeper electrode indentation meant smaller penetration of the liquid nugget, which can seriously deteriorate the welding quality. In addition, the worn electrode meant a rough surface of the electrode, so the local current density may be very large, which can easily induce surface expulsion. Hence, the electrode should be immediately repaired or replaced when it is worn.

3.4. Metallographic Observation and Measurement

In general, the nugget diameter was proportional to the tensile strength of the weld, so the majority of works employed the nugget diameter to estimate the welding quality.[1] In this work, detailed information on the weld can be obtained by means of metallographic observations, and then the results can be used to compare with those of numerical calculations. **Figure 15** shows a comparison between images of the cross section of nuggets obtained after a series of metallographic processes and from numeri-

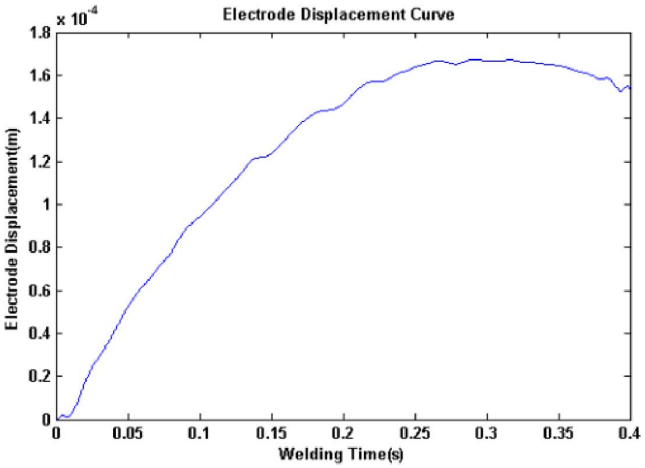

Fig. 14. Electrode displacement obtained from a worn electrode. (Online version in color.)

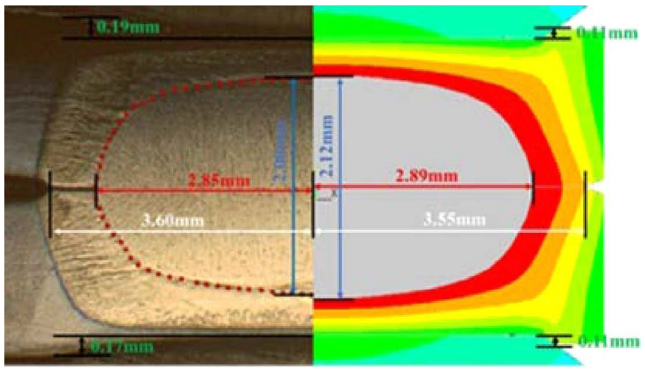

Fig. 15. A comparison of images of cross sections of nuggets obtained between metallographic processing and numerical calculation. (Online version in color.)

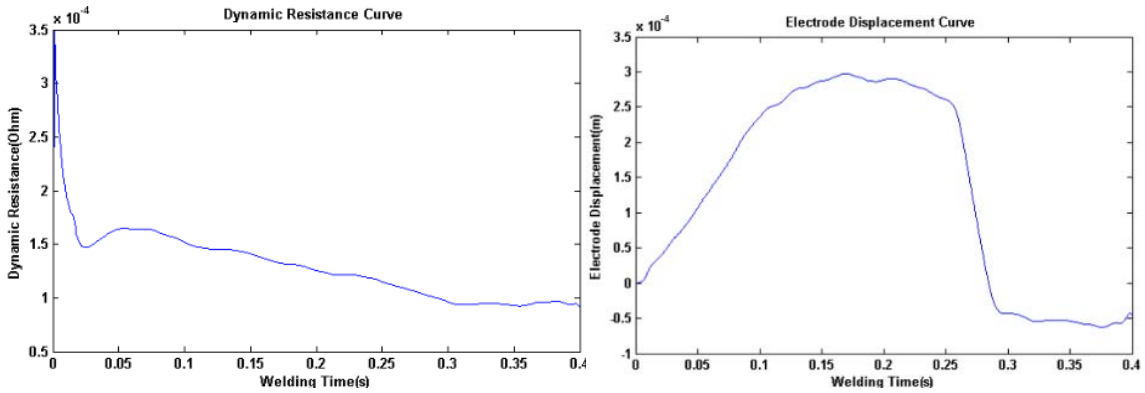

(a) (b)

Fig. 13. Process signal variation when expulsion occurred. (Online version in color.)

cal calculations. In the figure, a liquidus temperature line was employed to distinguish the solid and molten metals, so the liquid nugget can be clearly examined and measured. To obtain clear comparison results, corresponding measurement values were also added to the figure.

In the right part which was from numerical calculation, the gray part denoted the liquid nugget. **Table 3** showed the measurement results.

Where the penetration, which was also called the thickness, was the total length between the upper and lower boundaries of the nugget.

In addition, electrode indentation can also be an indicator to evaluate the weld quality.[33] There were many factors affecting the depth of electrode indentation, such as the diameter of the electrode, electrode force, welding current, and welding time. A large value of the depth of the electrode indentation can affect the range of the heat affected zone (HAZ), which means that the HAZ might not be able to contain the molten metal, and then expulsion or other forms of molten metal leakage might occur, which can decrease the nugget size, and corresponding weld quality was also significantly deteriorated.

In general, the electrode indention, nugget thickness and electrode displacement should follow Eq. (12), and the preceding two items of Eq. (12), which was the linear thermal expansion of the two electrodes and two parent metal sheets, can be denoted as h and d. The corresponding equation can be written in the following form:

$$S = 2h + 2d - 2S_{EF}. \quad \text{..... (14)}$$

In this work, after 0.30 s of welding time, the actual S was 0.33 mm, $2d$ was 2.00 mm, while in the numerical calculation, these two parameters were 0.31 mm and 2.12 mm, so the corresponding errors were −0.02 mm and 0.12 mm, respectively. Because the error of the linear thermal expansion of electrodes between the numerical calculation and experiment was very small, it can be ignored in this analysis. Therefore, the error of S_{EF} was −0.02 mm − 0.12 mm = −0.14 mm. This meant that the S_{EF} obtained from the numerical calculation was smaller than that obtained from the actual experiment, and the error was 0.14 mm. According to Fig. 15, S_{EF} in the upper and lower parent metals obtained from experiment were 0.19 mm and 0.17 mm, respectively, while in the numerical calculation the two values were both 0.11 mm, so the error of this parameter was also 0.14 mm in total. Therefore, in the numerical calculation, a certain calculation result will also affect other numerical calculation results, just as the indentation value in the above calculation can influence the calculation of electrode displacement. In the actual experiment, the electrode indentation in the upper and lower parent metal sheets had a small difference, which may because the upper and lower electrodes cannot be precisely the same, or the movements of these two electrodes were different in reality.

Table 3. Nugget size measurement from metallographic processing and images obtained from numerical calculation.

Nugget Parameter	Metallographic measurement (mm)	Numerical Calculation (mm)	Error (%)
Diameter	5.70	5.78	1.40
Penetration	2.00	2.12	6.00

In addition, the diameter of the contact area between two parent metal sheets can also be measured by metallographic observation and measurement. The corresponding variation in the numerical calculation is shown in Fig. 11, in which the final value was 7.10 mm, and the actual measurement was 7.20 mm in Fig. 15; the error was only 1.41%. This was a reason that the dynamic resistance in the actual experiment was lower than that of the numerical calculation in the last stage.

According to the above aspects of comparison and corresponding analyses, the results of the numerical calculation approached those obtained from metallographic observation and measurement very much. Therefore, the numerical calculation can well simulate the actual experimental process.

In this work, to achieve the goal of analyzing the characteristic variations in real time during different stages of the RSW process, a 2D thermal-electric-mechanical coupled FE numerical calculation model was employed. Though the numerical simulation was carried out under one condition, it may be also used extensively in many other conditions through some proper and targeted amendments. The model was based on basic working principles of RSW process, the main parameters, such as welding operational parameters and material characteristic parameters, can be easily to change into other ones to adapt to different welding conditions. For example, it may be used to simulate the conditions of electrode wearing by means of changing the values of friction coefficient and corresponding calculation of r_c in Eq. (5), if possible, the shape of electrodes in the model may also be changed. Also, by means of changing load mode of the welding current, different energy delivering modes of RSW operation with different values of welding current will be simulated using this model. Moreover, the model is also expected to simulate the RSW process with different materials, such as aluminum and steel, or the parent metal sheets having different electrical characteristics by correspondingly changing the material characteristics setting, such as electric resistivity, density, thermal conductivity, heat capacity, liquidus temperature, and other relative parameters, such as friction coefficient, r_c, and so on.

4. Conclusion

Process signals, such as dynamic resistance and electrode displacement, were important in welding quality estimation and online control strategy design during the RSW process. However, although FE numerical calculation is commonly employed to analyze the variation in metal characteristics during the RSW process, few works have considered the process signals. Under those circumstances, the calculation results of the FE model can only be compared with experimental results after the post-processing stage, which significantly limits its application and merit. In this work, a 2D multi-field coupled FE numerical calculation model was established to simulate the RSW process and compared with the process signals obtained from actual experiments. The meshing and key parameter arrangement were conducted by combining the characteristics of the FE model and RSW process. The numerical calculation process was composed

of 150 cycles and each cycle included a mechanical field model calculation and a thermo-electrical coupled field model calculation. By means of this numerical calculation model, the variations in dynamic resistance and electrode displacement can be explained by contact features, metal thermal linear expansion, and so on. Because process signals can be compared during all the welding process which includes different stages, and their characteristic variations can be sufficiently explained by combining the results from numerical calculation and actual experiment, the application of FE numerical calculation was effectively extended. Additionally, expulsion and electrode worn were also considered by combining the characteristics of process signals, and nugget size and electrode indentation were seriously measured by metallographic processing. A series of observations and comparisons validated the reliability and accuracy of the FE model and actual experiment. By means of this work, not only the understanding of detailed characteristics of process signals but also the adaptability of the FE model in actual RSW operation can be strengthened. It is anticipated that the work will be able to promote the application of the FE model in serving actual welding quality estimation or control strategy design of the RSW process.

Declaration of Competing Interest

The authors declare no competing interests.

Acknowledgments

The authors would like to thank the National Natural Science Foundation of China, China (Grant No: 51605103) and Beijing Institute of Technology Research Fund Program for Young Scholars, China (Grant No: 3020012222008).

REFERENCES

1) K. Zhou and P. Yao: *Mech. Syst. Signal Process.*, **124** (2019), 170. https://doi.org/10.1016/j.ymssp.2019.01.041
2) Y. Li, Z. Lin, Q. Shen and X. Lai: *J. Manuf. Sci. Eng.*, **133** (2011), 031019. https://doi.org/10.1115/1.4004319
3) X. Wang and K. Zhou: *IEEE-ASME Trans. Mechatron.*, **26** (2021), 1791. https://doi.org/10.1109/TMECH.2021.3075479
4) Y. Xia, Y. Shen, L. Zhou and Y. Li: *J. Manuf. Sci. Eng.*, **143** (2021), 031008. https://doi.org/10.1115/1.4048441
5) D. W. Zhao, Y. X. Wang, L. Zhang and P. Zhang: *Mater. Des.*, **50** (2013), 72. https://doi.org/10.1016/j.matdes.2013.02.016
6) P. Banerjee, R. Sarkar, T. K. Pal and M. Shome: *J. Mater. Process. Technol.*, **238** (2016), 226. https://doi.org/10.1016/j.jmatprotec.2016.07.023
7) P. S. Wei and T. H. Wu: *Int. J. Therm. Sci.*, **86** (2014), 421. https://doi.org/10.1016/j.ijthermalsci.2014.07.016
8) I. Iatcheva, D. Darzhanova and M. Manilova: *Open Phys.*, **16** (2018), 1. https://doi.org/10.1515/phys-2018-0001
9) Y. Li, Z. Lin, S. J. Hu and G. Chen: *J. Appl. Phys.*, **101** (2007), 053506. https://doi.org/10.1063/1.2472279
10) K. Zhou and L. Cai: *IEEE-ASME Trans. Mechatron.*, **19** (2014), 559. https://doi.org/10.1109/TMECH.2013.2251351
11) P. Podržaj, I. Polajnar, J. Diaci and Z. Kariž: *Sci. Technol. Weld. Join.*, **13** (2008), 215. https://doi.org/10.1179/174329308X283893
12) J. Wen, H. D. Jia and C. S. Wang: *ISIJ Int.*, **59** (2019), 2073. https://doi.org/10.2355/isijinternational.ISIJINT-2019-002
13) O. L. R. Ighodaro, E. Biro and Y. N. Zhou: *Metall. Mater. Trans. A*, **48** (2017), 745. https://doi.org/10.1007/s11661-016-3899-3
14) X. Wan, Y. Wang and D. Zhao: *ISIJ Int.*, **58** (2018), 721. https://doi.org/10.2355/isijinternational.ISIJINT-2017-282
15) L. Zhou, Y. Xia, Y. Shen, A. S. Haselhuhn, D. M. Wegner, Y. Li and B. E. Carlson: *J. Manuf. Process.*, **63** (2021), 98. https://doi.org/10.1016/j.jmapro.2020.03.061
16) K. Zhou and L. Cai: *J. Appl. Phys.*, **115** (2014), 164901. https://doi.org/10.1063/1.4872247
17) K. Zhou and H. Li: *IEEE Access*, **8** (2020), 107260. https://doi.org/10.1109/ACCESS.2020.3000794
18) M. Eshraghi, M. A. Tschopp, M. A. Zaeem and S. D. Felicelli: *Mater. Des.*, **56** (2014), 387. https://doi.org/10.1016/j.matdes.2013.11.026
19) J. Wang, H. Wang, F. Lu, B. E. Carlson and D. R. Sigler: *Int. J. Heat Mass Transf.*, **89** (2015), 1061. https://doi.org/10.1016/j.ijheatmasstransfer.2015.05.086
20) M. Vural: *Usak Univ. J. Mater. Sci.*, **2** (2013), 31.
21) H. Moshayedi and I. Sattari-Far: *J. Mater. Process. Technol.*, **212** (2012), 347. https://doi.org/10.1016/j.jmatprotec.2011.09.004
22) Y. Wang: Master thesis, School of Materials Science and Engineering Jilin University, (2018) (in Chinese).
23) W. Wang: Master thesis, School of Materials, Shanghai Jiao Tong Univerisity, (2017) (in Chinese).
24) M. Hamedi and M. Atashparva: *Weld. World*, **61** (2017), 269. https://doi.org/10.1007/s40194-016-0419-4
25) Professional Committee of Resistance Welding, Welding Society of Chinese Mechanical Engineering Society (III): Theory and Practice of Resistance Spot Welding, China Machine Press, Beijing, (1994), 8 (in Chinese).
26) Z. Wan, H. Wang, M. Wang, B. E. Carlson and D. R. Sigler: *Int. J. Heat Mass Transf.*, **101** (2016), 749. https://doi.org/10.1016/j.ijheatmasstransfer.2016.05.023
27) D. Zhao, D. Ren, G. Song, K. Zhao, L. Liu and Z. Zhang: *Int. J. Mech. Sci.*, **187** (2020), 105933. https://doi.org/10.1016/j.ijmecsci.2020.105933
28) W. Zhang: *SAE Int. J. Mater. Manuf.*, **112** (2003), 556. https://doi.org/10.4271/2003-01-0978
29) Z. Hou, I.-S. Kim, Y. Wang, C. Li and C. Chen: *J. Mater. Process. Technol.*, **185** (2007), 160. https://doi.org/10.1016/j.jmatprotec.2006.03.143
30) K. Zhou, P. Yao and L. Cai: *J. Mater. Process. Technol.*, **223** (2015), 299. https://doi.org/10.1016/j.jmatprotec.2015.04.016
31) W. Tan, Y. Zhou, H. W. Kerr and S. Lawson: *J. Phys. D: Appl. Phys.*, **37** (2004), 1998. https://doi.org/10.1088/0022-3727/37/14/017
32) Y. Xia, Z. Su, Y. Li, L. Zhou and Y. Shen: *J. Manuf. Process.*, **46** (2019), 34. https://doi.org/10.1016/j.jmapro.2019.08.004
33) Y. Xia, L. Zhou, Y. Shen, D. M. Wegner, A. S. Haselhuhn, Y. Li and B. E. Carlson: *Measurement*, **168** (2021), 108397. https://doi.org/10.1016/j.measurement.2020.108397